Science Advances
AAAS

advances.sciencemag.org/cgi/content/full/7/16/eabe8210/DC1

Supplementary Materials for

Effect of mesoscale phase contrast on fatigue-delaying behavior of self-healing hydrogels

Xueyu Li, Kunpeng Cui, Takayuki Kurokawa, Ya Nan Ye, Tao Lin Sun, Chengtao Yu, Costantino Creton, Jian Ping Gong*

*Corresponding author. Email: gong@sci.hokudai.ac.jp

Published 14 April 2021, *Sci. Adv.* **7**, eabe8210 (2021)
DOI: 10.1126/sciadv.abe8210

The PDF file includes:

Other Supplementary Material for this manuscript includes the following:

(available at advances.sciencemag.org/cgi/content/full/7/16/eabe8210/DC1)

1. Methods

1.1 Synthesis of polyampholyte hydrogels (PA gels)

The charge-balanced polyampholyte hydrogels (PA gels) were synthesized by one-step random copolymerization following the procedure in ref (*7, 46*). Briefly, a mixed precursor aqueous solution of NaSS, DMAEA-Q, α-keto, and MBAA was injected into a reaction cell (20 cm× 20 cm) consisting of a pair of glass plates with a 2 mm silicone spacer. In the precursor aqueous solution, an optimized molar fraction f=0.515 [f=(NaSS)/C_m, C_m is the total monomer concentration] was applied, and the content of initiator α-keto was 0.1 mol %. Polymerization was carried out in argon atmosphere keeping the oxygen concentration less than 0.1 ppm by irradiating UV light (wavelength 365 nm, light intensity ~4 $mWcm^{-2}$) from both sides of the reaction cell for 11 h. After polymerization, the as-prepared gels were dialyzed in de-ionized water for 3 weeks to remove the counter ions and reach equilibrium. Unless specified, the dialysis temperature (T_{dial}) was kept at 30 ℃. To tune the hierarchical structures of the PA gels, two series of samples were prepared. One was samples with different cross-linker content (C_{MBAA}) while the monomer concentration (C_m) was kept at 2.5 M (PA-2.5-C_{MBAA}); another was samples with different C_m while the C_{MBAA} was kept at 0.1 mol % (PA-C_m-0.1). The former tuned effective cross-linking density of the permanent polymer network v_e by chemical cross-linking, and the later tuned the v_e by trapped topological entanglement, as indicated in (*24*). The sample code, formulation, fabrication condition, structure and properties of samples used in this work are shown **Table S1**. The thickness of the equilibrated gels is t_0~1.65 mm.

1.2 Toughness measurement

The fracture energy of gels was obtained from a pure shear test. Two different samples, single-edge notched and unnotched, were used to measure the fracture energy Γ. Unless specified, the sample with a pure shear geometry (50 mm×10 mm×1.65 mm, L_0×H_0×t_0) was mounted in a tensile tester

(Shimadzu Autograph AG-X tensile machine) with a 100 N load cell. For the notched sample, the initial notch c_0 was 10 mm (**Fig. 3A**). During the test, the water vapor was sustainably supplied around the gels. The experiment temperature was kept constant at 24°C, and the nominal loading stretch rate was 1 s^{-1}. The force-displacement curves of the samples were recorded. The toughness Γ was calculated from

$$\Gamma = U(H_c)/(L_0 \times t_0), \quad \text{(SM-1)}$$

Where $U(H_c)$ is the work done by the applied force to the unnotched sample at critical stretching distance H_c (the distance when crack starts to propagate on notched sample).

1.3 SAXS measurement

The bicontinuous hard/soft phase networks were characterized by small-angle X-ray scattering (SAXS), which was carried out at the Synchrotron Radiation Facility (BL19U2, Shanghai, China). The X-ray wavelength used was 1.03 Å. A two-dimensional detector (Pilatus 1M with a resolution of 981×1043 pixels and pixel size of 172 μm, Dectris Co. Ltd) was used to record data. The sample-to-detector distance was 5730 mm. The exposure time was 2 s for the undeformed gels.

For time-resolved SAXS measurements during uniaxial tensile loading, a tensile machine with well controlled humidity and temperature (Hefei Puliang Technology Co., Ltd) was used. To get the whole deformation information, unnotched rectangular samples (7.5 mm×16 mm×1.65 mm, $L_0 \times H_0 \times t_0$, see inset of **Fig. S3A**) were applied, for which, the microscopic deformation follows $\lambda_1=\lambda$ (parallel to stretching direction), $\lambda_2=\lambda_3=\lambda^{-1/2}$ (sample width and thickness direction) under affine deformation for incompressible material (*48*). The nominal loading stretch rate was controlled to be 1 s^{-1}. Experimental temperature was 24 ℃. 2D SAXS patterns were acquired at a rate of 0.25 s/frame. The resulting strain, stress and SAXS patterns were recorded.

Fit 2D software from the European Synchrotron Radiation Facility was used to analyze the SAXS data. The background scattering from the air was subtracted from the data. The 2D SAXS

patterns were integrated along the azimuthal direction to obtain 1D scattering profiles as a function of the scattering vector

$$q=4\pi\sin\theta/\lambda, \quad \text{(SM-2)}$$

where q is the module of scattering vector, λ is the X-ray wavelength, and 2θ is the scattering angle. The distance between adjacent hard (soft) phases (characteristic distance of the phase structure, d) was obtained from the position of the scattering maxima q_m according to Bragg's law

$$d=2\pi/q_m. \quad \text{(SM-3)}$$

1.4 Fatigue test

The fatigue experiments were performed using the Shimadzu tensile tester (AG-X, Shimadzu corporation), and notched samples with the pure shear geometry were used (**Fig. 3A**), unless otherwise mentioned. To prevent samples from dehydrating, a humidity chamber was set on the tensile tester, where water vapor was sustainably supplied. The weight change of sample before and after fatigue test was within 2 wt%. Cyclic loading-unloading was performed along the sample height H_0 direction. During fatigue tests, the maximum elongation ratio in each cycle held at λ_{max}, and the minimum held at $\lambda=1$, at constant temperature 24 ℃. A digital camera (canon 7D) was used to record photos during crack extension for notched samples every 10 min and every 1 min for samples with slow and fast crack growth, respectively (the extension length was recorded as c). The crack propagation rate $\Delta c/\Delta N$ was obtained from the slope of the plots of crack length c versus cycle number N in steady state. To improve the reliability of results, several representative values of λ_{max} were tested for at least two times. The amplitude of load in terms of the energy release rate G was calculated from

$$G=W_{el}(\lambda_{max})H_0, \quad \text{(SM-4)}$$

where H_0 is the initial distance between the two clamps, $W_{el}(\lambda_{max})$ is the elastic strain energy density of unnotched sample (the same kind of geometry for fatigue test) in steady state (**Fig. S4E**).

1.5 Birefringence test

To observe the stress distribution, a homemade circular polarizing optical system (*47*) was applied to the fatigue test for several representative samples. In brief, notched sample in the pure shear geometry (**Fig. 3A**) or notched rectangular samples (**Fig. S7A**) were fixed on the tensile tester. Before cyclic loading, a video camera and a white LED light panel were installed on the front side and back side of the sample, respectively. A circular polarizer film was fixed on the lens of the camera and another one was fixed on the light panel. During cyclic loading, the shape and isochromatic images were recorded by the camera.

2. Structures and mechanical properties of PA gels

2.1 Network structure analysis

The storage modulus G' at ~2×10^{-5} rad/s, where the plateau (quasi-plateau for no cross-linking and lightly cross-linked gels) of G' appeared (**Fig. S1**), was taken as the shear modulus μ to calculate the effective cross-linking chain density per unit volume of the permanent network ν_e, since at such a low frequency, the contribution of the transient network to shear modulus by the reversible ionic bonds is negligible (**Fig. S1**).

$$\nu_e=\mu/(kT), \tag{SM-5}$$

where k is the Boltzmann constant, and T is the absolute temperature (297.15 K). The ν_e thus obtained should account for the chains cross-linked chemically by cross-linker and physically by trapped topological entanglements.

The molar mass of polymer strands between effective cross-linking points $M_{x,eff}$ is related to the shear modulus μ as (*26*)

$$\mu=\nu_e kT=\rho\phi RT/M_{x,eff}, \tag{SM-6}$$

here, ρ, ϕ, R, and T are dry polymer density(g/m^3), polymer volume fraction in gel, the gas constant (J/mol K), and temperature (K), respectively. Note that the polymer volume fraction ϕ is nearly constant (~46 vol%), so $M_{x,eff}$ is inversely proportional to v_e. $M_{x,eff}$ is related to the molecular mass between chemical cross-links and topological entanglements, M_x and M_e, respectively, as $1/M_{x,eff} = 1/M_x + 1/M_e$.

Since the volume of one strand between the effective cross-linking points is $1/v_e$, so v_e correlates to the nano-scale mesh size of polymer network ξ by $v_e \cong \xi^{-3}$. Thus, we can get ξ from the value of v_e. The v_e, $M_{x,eff}$ and ξ for samples prepared at various formulations are shown in **Table S1**.

Table S1. Formulation of PA gels used in this work and characteristics of the structures formed. C_m, C_{MBAA}, and T_{dial} are total monomer concentration, cross-linker concentration in relative to monomer, and dialysis temperature, respectively. The ϕ is the polymer volume fraction, and μ is the storage shear modulus at 2×10^{-5} rad/s of the gels. v_e is effective cross-linking chain density per unit volume. $M_{x,eff}$ is molar mass of polymer strands between effective cross-linking points, and ξ is nano-scale mesh size of permanent polymer network. The ϕ, μ, v_e, $M_{x,eff}$, and ξ are average values of three tests. PA-2.0-0.1 (T_{dial}) are samples applied in ref (*25*). For brief, PA-2.0-0.1 also denotes PA-2.0-0.1 (T_{dial}=30 ℃).

Sample code PA-C_m-C_{MBAA}(T_{dial})	C_m (M)	C_{MBAA} (mol %)	T_{dial} (℃)	ϕ (vol%)	μ (kPa)	v_e (10^{24}/m^3)	$M_{x,eff}$ (10^3 g/mol)	ξ (nm)
PA-2.5-0	2.5	0	30	46.2	8.1	1.97	197.5	7.98
PA-2.5-0.075	2.5	0.075	30	46.8	6.3	1.54	260.0	8.67
PA-2.5-0.1	2.5	0.1	30	45.8	13.9	3.38	114.9	6.67
PA-2.5-0.2	2.5	0.2	30	45.1	18.3	4.47	86.6	6.08
PA-2.5-0.5	2.5	0.5	30	46.5	27.4	6.67	56.9	5.31
PA-2.5-1	2.5	1	30	46.1	45.3	11.1	35.3	4.49
PA-2.0-0.1	2.0	0.1	30	44.8	8.8	2.14	180.7	7.79
PA-1.75-0.1	1.75	0.1	30	44.7	7.9	1.94	209.7	8.10
PA-2.0-0.1(5 ℃)	2.0	0.1	5	46.1	8.0	1.94	200.0	8.04
PA-2.0-0.1(60 ℃)	2.0	0.1	60	45.4	7.7	1.88	207.7	8.11

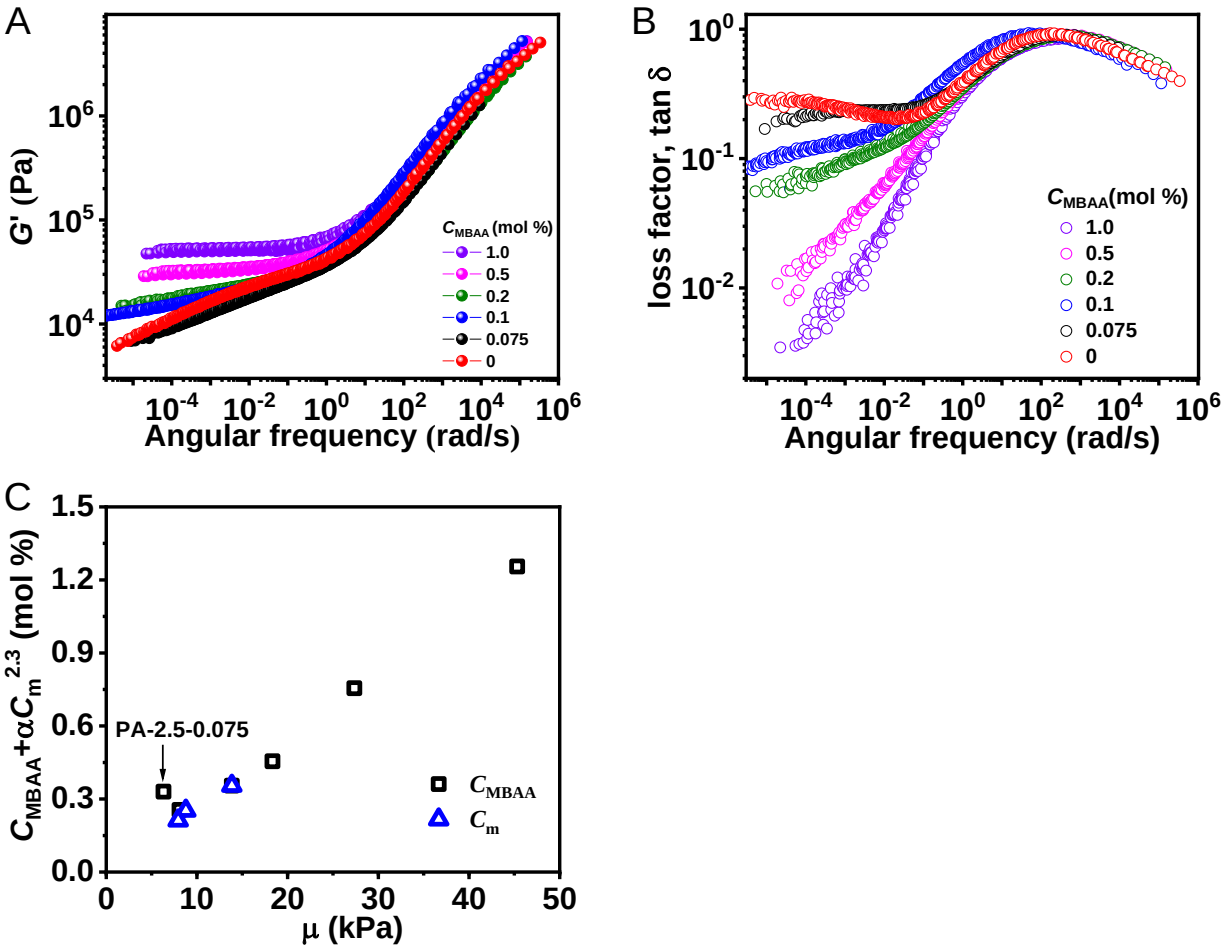

Fig. S1. Dynamic mechanical behavior, as well as dependence of the plateau elastic modulus on chemical cross-linker density and monomer concentration. (A, B) Dynamic mechanical behavior of PA-2.5-C_{MBAA}. Constructed master curves for frequency dependence of (A) storage modulus (G') and (B) loss factor (tan δ) at a reference temperature of 25 ℃ by following the principle of time-temperature superposition. It shows that the effect of ionic bonds on the dynamic mechanical behavior mainly occurs at angular frequency larger than 10^{-1} rad/s. The G' at low frequency regime is mainly contributed from effective cross-linking networks, from both chemical cross-linking and permanent topological entanglement. We used G' at 2×10^{-5} rad/s as plateau elastic modulus μ (**Table S1**) for calculation of the effective cross-linking structure of the permanent networks. A characteristic relaxation time of ~20 ms, which represents the exchange time of most of the weak bonds (*46*), can be obtained from the frequency at the peak of loss factor (300 rad/s). (**C**) Relation between the shear modulus μ estimated from plateau elastic modulus and the chemical cross-linker density C_{MBAA} and monomer concentration C_m. The same fitting constant reported in literature (*24*) α=0.031 mol %·$M^{-2.3}$ is used.

Table S2. A summary of the structural parameters and λ_{affine} of PA gels prepared with different chemical cross-linker densities (C_{MBAA}) and monomer concentrations (C_m) at the dialysis temperature (T_{dial}) of 30°C, as well as PA-2.0-0.1 dialyzed at different temperature T_{dial}. The data of PA-2.0-0.1(T_{dial}) is extracted from ref (*25*). The SAXS scattering intensity I_m is related to phase density contrast $\Delta\rho$ by $I_m \propto \Delta\rho^2$ as indicated in (*24*).

Sample code PA-C_m-C_{MBAA}(T_{dial})	d_0 (nm)	I_m (arb.unit)	λ_{affine}
PA-2.5-0	213.5	349.4k	--
PA-2.5-0.075	104.7	19.6k	3.27
PA-2.5-0.1	79.1	8.7k	2.54
PA-2.5-0.2	48.1	0.56k	1.90
PA-2.5-0.5	37.3	0.26k	--
PA-2.5-1	--	--	--
PA-2.0-0.1	101.3	14.7k	3.06
PA-1.75-0.1	148.7	52.5k	3.65
PA-2.0-0.1(5 ℃)	95.4	9.5k	2.82
PA-2.0-0.1(60 ℃)	103.8	21.3 k	3.52

Note that the physical gel without chemical cross-linking, PA-2.5-0, shows the largest I_m and d_0, that is close to detection limit of SAXS we used, and we could not get an accurate value of λ_{affine}. The scattering intensity of weakly phase-separated PA-2.5-0.5 was too weak, so we also could not get the λ_{affine}. The PA-2.5-1.0 did not show scattering peak indicating that phase-separated structure was not formed.

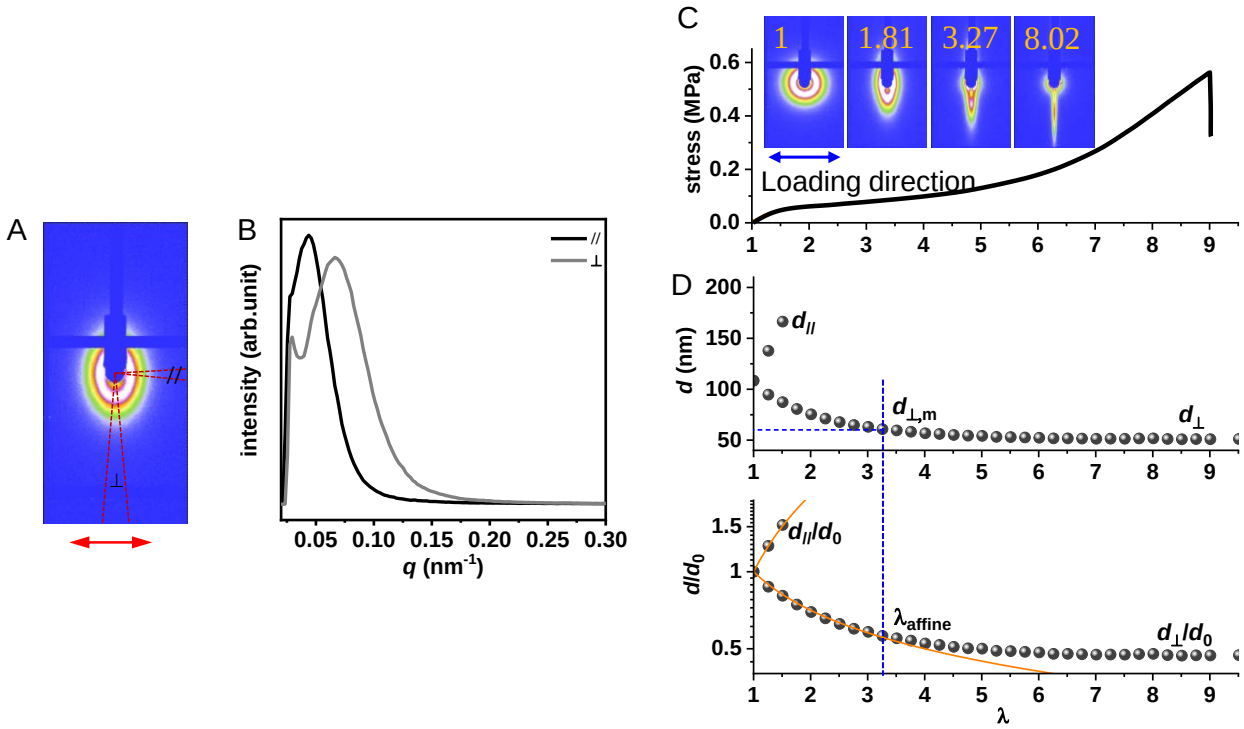

Fig. S2. Method to get the microscopic deformation of phase networks. PA-2.5-0.075 is taken as an example. (**A**) The parallel (//) and perpendicular (⊥) sector regions for integrating the 1D scattering intensity for deformed sample, and (**B**) the corresponding integrated 1D SAXS profiles. The loading direction of sample is indicated by red arrow. The characteristic distance of deformed bicontinuous phase networks (d) is calculated from the peak position of 1D SAXS profiles (q_m), by $d=2\pi/q_m$. $d_{//}$ and $d_{\perp}$ represent characteristic distance in parallel and perpendicular to loading direction, respectively. (**C**) Tensile stress–stretch ratio (λ) curve of strongly phase-separated PA-2.5-0.075. Inset shows that the 2D SAXS patterns elongate with stretch ratio in the perpendicular direction, indicating the elongation and compression of the phase networks in parallel and perpendicular directions, respectively, during loading. (D) Evolution of $d_{//}$ and $d_{\perp}$ with stretch ratio λ (upper). The lower shows the evolution of microscopic deformation $d_{//}/d_0$ and $d_{\perp}/d_0$ with λ. The orange lines stand for the prediction of affine deformation of the phase networks ($d_{//}/d_0=\lambda$ and $d_{\perp}/d_0=\lambda^{-1/2}$ for incompressible materials). The $d_{//}$ exceeds detecting range at $\lambda>1.7$, while the $d_{\perp}$ can be detected over the whole λ range until the fracture of the sample. The maximum stretch ratio for affine deformation (λ_{affine}) of phase networks, is identified as the point where the microscopic deformation starts to deviate from macroscopic deformation λ. At $\lambda<\lambda_{affine}$, the bicontinuous phase networks keep intact and deform affinely; while at $\lambda>\lambda_{affine}$, the phase network deformation becomes inhomogeneous deformation, and stress concentration occurs (*23*). We can see from the evolution of $d_{\perp}/d_0$ that the λ_{affine} of phase networks is $\lambda_{affine}=3.27$ for this sample, and the corresponding characteristic distance in parallel direction is $d_{//,m}=\lambda_{affine}d_0$. Note that we cannot measure the d-spacing change for a sample in a pure shear geometry since the lateral deformation is constrained and $d_{\perp}$ is always equal to d_0 in the case of a pure shear geometry (*49*). Therefore, we used the rectangular samples (inset of **Fig. S3A**) to get SAXS results. Initial loading strain rate was 1 s^{-1}.

2.2 Tensile and fracture behaviors

Fig. S3 shows the tensile and fracture behavior for PA-2.5-C_{MBAA} and PA-C_m-0.1. The tensile test was performed using a rectangular sample (inset of **Fig. S3A**) while the fracture test was performed using prenotched samples in the pure shear geometry (inset of **Fig. S3C**). Although the phase structure of the gels with C_{MBAA}≤0.1 mol % is significantly different, they exhibit little difference in uniaxial tensile behavior (**Figs. S3A**, **S3E**) and in fracture behavior in the pure shear geometry (**Fig. S3C**). For gels with C_{MBAA}>0.1 mol %, the mechanical behaviors are largely different for different C_{MBAA}. The stretch ratio λ at fracture and the toughness decrease with increasing C_{MBAA} (**Figs. S3A**, **3C**, **3D**). While sample with C_{MBAA}≤0.1 mol % have a pronounced softening at intermediate λ, the sample with C_{MBAA}>0.1 mol % do not soften much and have an early strain hardening that should be related to the dense cross-linking.

The change in characteristic distance d_0 during the uniaxial extension, which reflects the deformation of the bicontinuous phase networks of PA gels, was measured by time-resolved SAXS. The analysis method was shown in **Fig. S2**. The phase separation of the samples PA-2.5-0.5 and PA-2.5-1.0 are too weak to measure during tensile test, and the phase size of PA-2.5-0 is close to detection limit of SAXS. Thus, we did not get accurate data of these three samples. Other results are shown in **Figs. S3B**, **S3F.** Consistent with the results in ref.(*23*), the phase networks elongate with load and gradually become highly anisotropic (inset in **Fig. S2C**). All the tested gels show a wide range of affine deformation at the phase network scale, and the maximum stretch ratio for affine deformation of the phase networks (λ_{affine}), increases from 1.9 to 3.27 with C_{MBAA} decreasing from 0.2 mol % to 0.075 mol % (**Table S2**, **Fig. S3B**). Decreasing C_m while keeping C_{MBAA} constant also increases λ_{affine}, showing a similar effect with that of C_{MBAA}. Specifically, for the PA-C_m-0.1, the λ_{affine} increases from 2.54 to 3.65 with decreasing C_m from 2.5 M to 1.75 M (**Fig. S3F**). As previously discussed, we interpret the deviation from the affine deformation as the onset of stress concentration due to the damage of hard phase network (*25*).

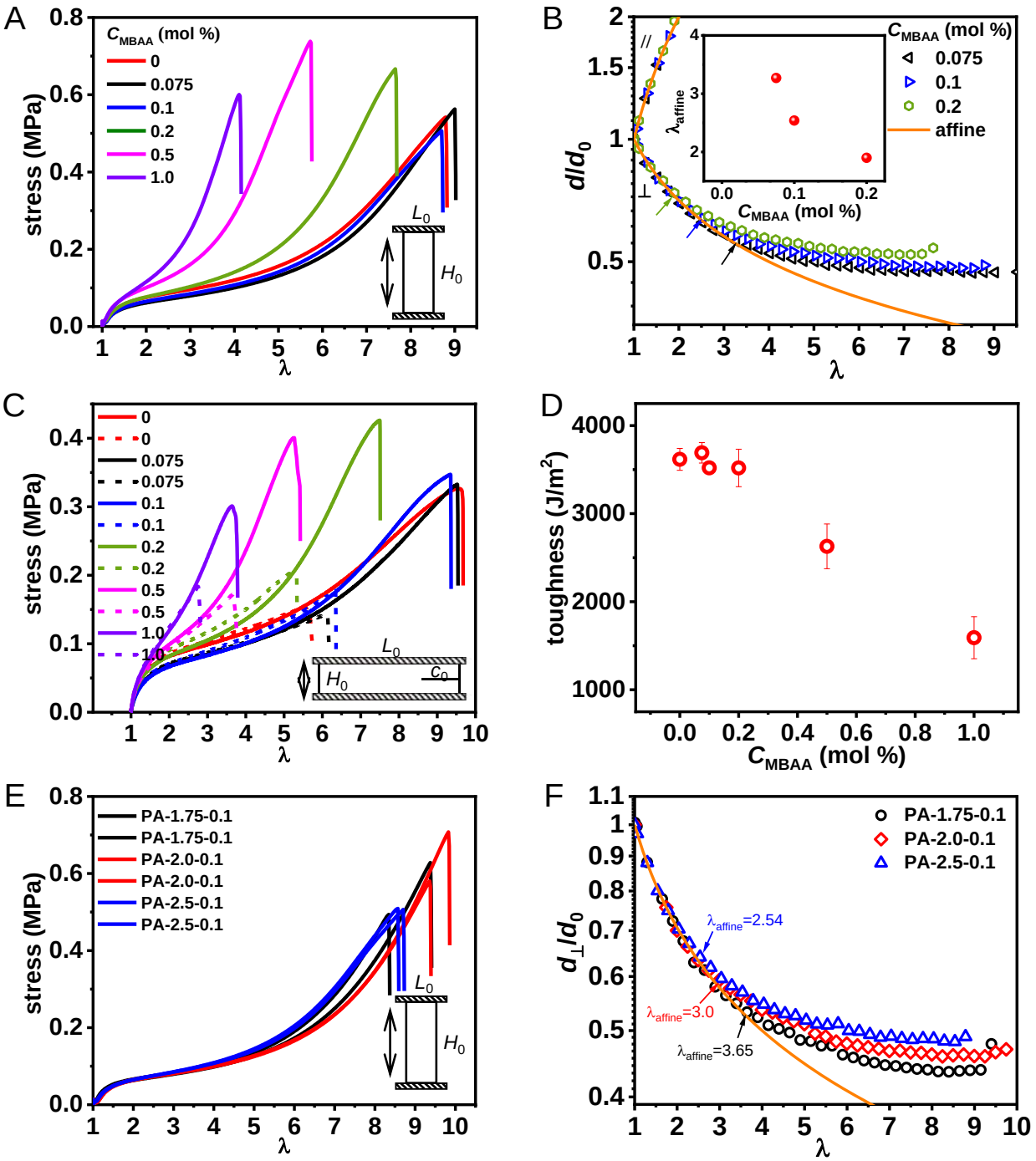

Fig. S3. Tensile and fracture behavior of PA gels with varied cross-linker density (PA-2.5-*C*MBAA) and monomer concentration (PA-*C*m-0.1). (**A-D**) Sample PA-2.5-*C*MBAA. (**A**) Tensile behaviors of the PA gels at a nominal strain rate 1 s^{-1}. (**B**) Phase network deformation ratio in parallel ($d_{//}/d_0$) and perpendicular ($d_⊥/d_0$) directions versus global elongation ratio λ for PA gels under uniaxial tensile deformation. The orange lines represent the prediction of affine deformation ($d_{//}/d_0=\lambda$ and $d_⊥/d_0=\lambda^{-1/2}$ for an incompressible material). The maximum λ for affine deformation of the phase network, λ_{affine}, where the $d_⊥/d_0$ deviates from the predicted affine deformation, is indicated by arrows with the corresponding colors. Inset shows the λ_{affine} as a function of C_{MBAA}. The geometry of the rectangular sample used in the tensile test and time-resolved SAXS measurement is shown in the inset of (A) (L_0=7.5 mm and H_0=16 mm). (**C**) Stress-λ curves for unnotched (solid line) and notched (dash line) sample in the pure shear test (L_0=50 mm and H_0=10 mm, c_0=10 mm and 0 for notched and unnotched sample, respectively). The stress has been

corrected by the effective initial area of cross section. The nominal strain rate is 1 s^{-1}. The legend represents the values of C_{MBAA}. (**D**) The fracture energy of PA gels determined from the pure shear test as a function of C_{MBAA}. The error bars are standard errors from 3 measurements. (**E-F**) Sample PA-C_m-0.1. (**E**) Uniaxial tensile behaviors of PA-C_m-0.1. For each composition, results from two specimens are shown. (**F**) Microscopic deformation of phase networks in perpendicular direction ($d_\perp/d_0$) with elongation ratio λ for PA-C_m-0.1. λ_{affine} is indicated by arrows.

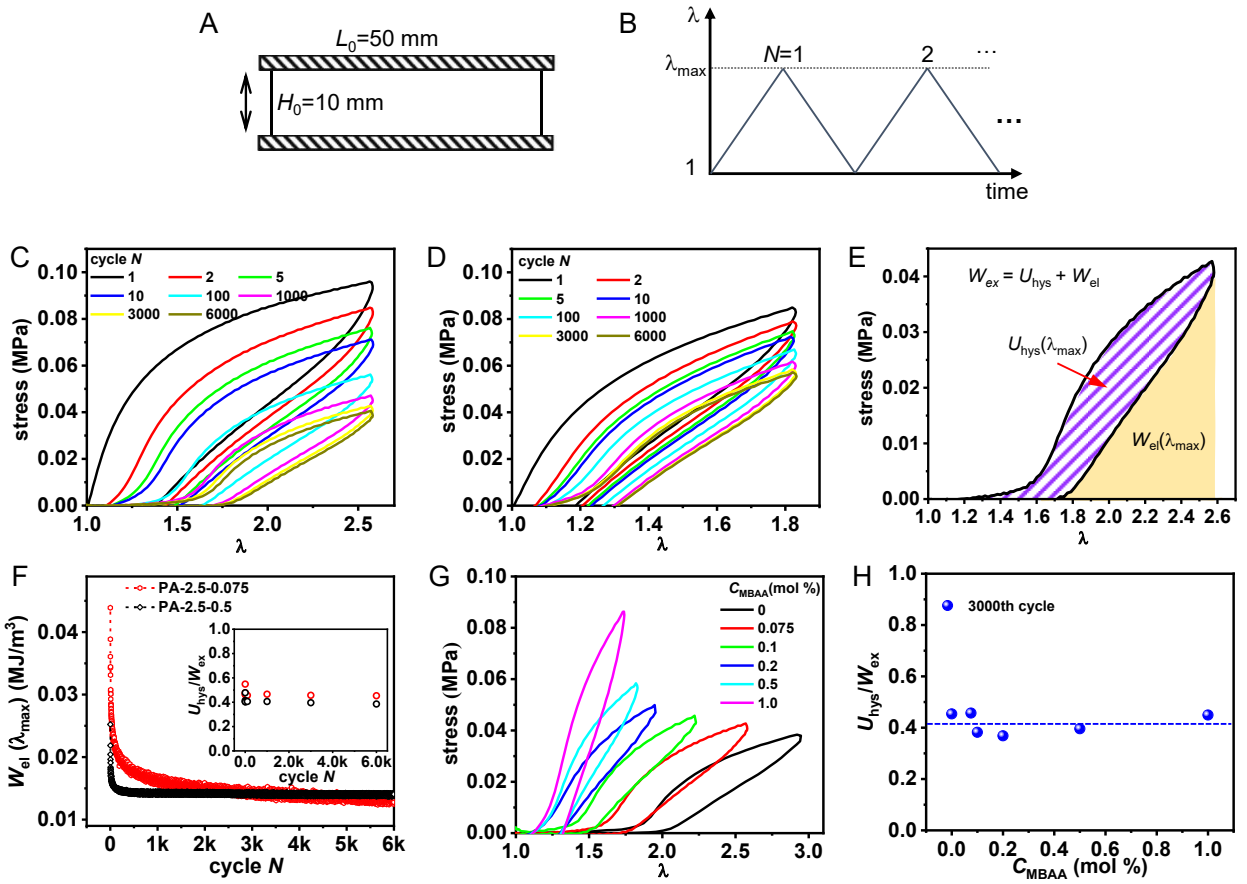

Fig. S4. Stress-stretch ratio (λ) curves for unnotched samples and method to obtain energy release rate *G*. (**A**) Unnotched sample with pure shear geometry used in this work to obtain the energy release rate G for the same kind of geometry (H_0=10 mm and L_0=50 mm). (**B**) Triangle loading profile for cyclic loading. To obtain the G for the crack propagation, the maximum (λ_{max}) and minimum elongation ratios, as well as nominal strain rate were the same with that applied for fatigue test. (**C**) Evolution of stress-λ curves with cycle number N at λ_{max}=2.57 for PA-2.5-0.075 as an example of the strongly phase-separated gels. (**D**) Evolution of stress-λ curves with cycle number N at λ_{max}=1.83 for PA-2.5-0.5 as an example of the weakly phase-separated gels. The energy release rate G for these two representative samples at the above λ_{max} was the same. Softening and shakedown were observed for both samples. After 3000 cycles, the change of stress with λ was negligible, and the samples are considered as in steady state. Large hysteresis loops [indicated by purple hatched lines in (**E**)] were observed even in steady state for both samples, indicating that the dissociation and association of ionic bonds reached an equilibrium under the working strain rate (1 s^{-1}). The energy release rate G was calculated by $G=W_{el}(\lambda_{max})H_0$, where the $W_{el}(\lambda_{max})$ is the elastic strain energy density of the unnotched sample in steady state [yellow area in (E)]. (**F**) The $W_{el}(\lambda_{max})$ as a function of cycle numbers N for PA-2.5-0.075 and PA-2.5-0.5 at λ_{max}=2.57 and 1.83, respectively, which also shows that the elastic strain energy density reaches steady state after 3000 cycles. Inset shows the ratio between hysteresis energy and the total input work U_{hys}/W_{ex} (both U_{hys} and W_{ex} are the values of the same cycle) as a function of cycle number N. U_{hys}/W_{ex} decreases slightly from 1st to 5th cycle, and then keeps constant at ~40%, indicating that the dissociation and reforming times of the ionic bonds are much shorter than the observation time scale. (**G**) Stress-λ curves in steady state (3000th cycle) for samples PA-2.5-C_{MBAA} with an energy release rate G ~150 J/m^2. Large hysteresis loops are observed for all the gels. (**H**) U_{hys}/W_{ex} in steady state (3000th cycle) for PA-2.5-C_{MBAA} with an energy release rate G~150 J/m^2. It shows that U_{hys}/W_{ex} in steady state keeps at ~40%, independent on C_{MBAA}, indicating that the ionic bonds play a same role on cyclic loading in steady state in strongly and weakly phase-separated gels.

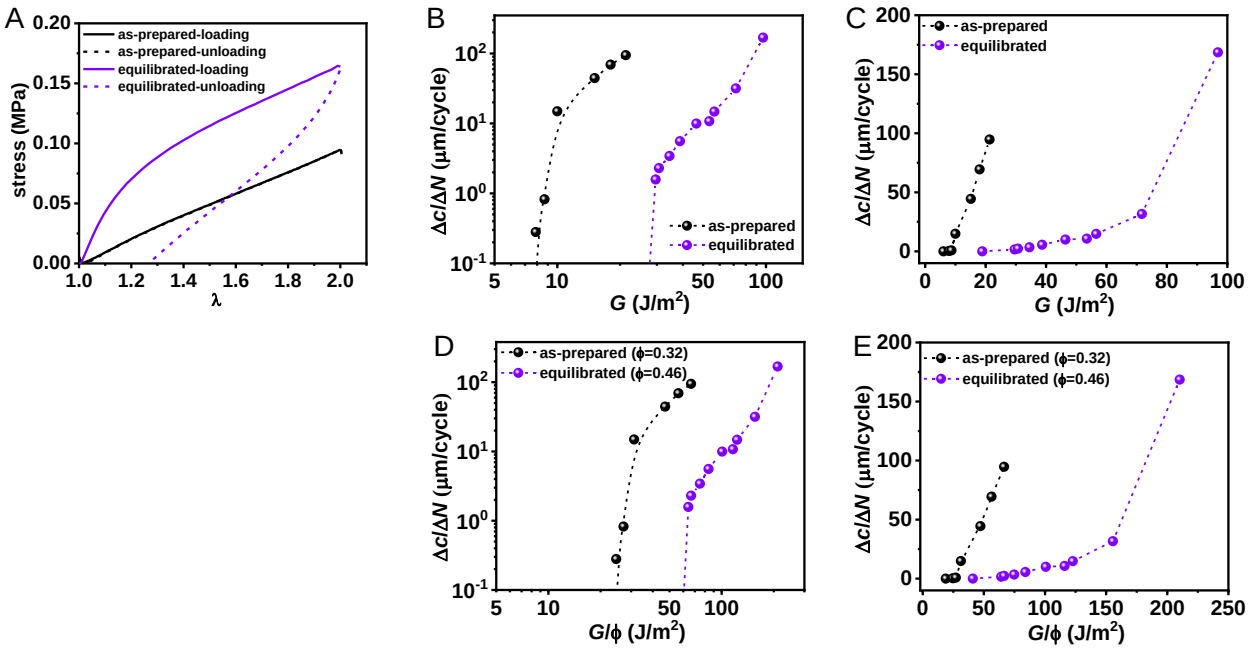

Fig. S5. Effect of ionic bonds on self-recovery and fatigue behavior. The as-prepared and equilibrated gels PA-2.5-1 are taken as an example. (**A**) Cyclic loading-unloading (first cycle) behavior of the as-prepared and equilibrated gels PA-2.5-1 at λ_{max}=2 under nominal strain rate 1 s^{-1}. (**B-C**) Crack propagation rate $\Delta c/\Delta N$ versus energy release rate G in logarithmic (B) and linear scale (C). In fatigue test, the measurements were performed with samples of pure shear geometry (L_0=50 mm, H_0=10 mm, and c_0=10 mm) and nominal strain rate 1 s^{-1}. The applied λ_{max} for fatigue test is λ_{max}=1.11 to 1.20 for the as-prepared gel, and λ_{max}=1.18 to 1.53 for the equilibrated gel. Since the as-prepared gel shows 30% volume shrinkage after dialyzed in water to equilibrated state, we also plotted the crack propagation rate $\Delta c/\Delta N$ versus G rescaled by polymer volume fraction ϕ by G/ϕ in logarithmic (**D**) and linear scale (**E**). Here, we adopted the linear relation between fracture threshold Γ_0 and ϕ, $\Gamma_0 \propto \phi$, as proposed in (*43*).

The polymer volume fraction ϕ of the equilibrated gel PA-2.5-1 was obtained by $\phi = 1 - \frac{c_w \rho_g}{\rho_w}$, where c_w is weight fraction of water (0.454), ρ_g is the density of the gel (~1.185±0.004 g cm^{-3}), and ρ_w is the density of water at 25 °C (~0.997 g cm^{-3}). The ϕ of the equilibrated PA-2.5-1 is estimated to be 0.46. The as-prepared gel has 30% volume shrinkage after dialyzed in water to remove the counterions and to reach equilibrated state. The ϕ of the as-prepared PA-2.5-1 is ϕ(as-prepared) = ϕ(equilibrated)×(100%-30%)/100%=0.32.

The fast self-recovery of PA gels under our fatigue test condition is reflected by the large hysteresis loops in steady state as shown in **Fig. S4,** caused by the reformation of ionic bonds during fatigue test. The as-prepared gel containing large amounts of counterions (these small ions screen the ionic bond formation between polymer chains) is elastic, not showing hysteresis loop (**Fig. S5A**). The fatigue-resistance of the as-prepared gel is weaker than the equilibrated gel that contains large amount of ionic bonds (**Fig. S5B-E**). The rescaled fatigue threshold G_0/ϕ are 23.6 J/m^2 and 41 J/m^2 for the as-prepared gel and equilibrated gel, respectively. Moreover, above the G_0/ϕ, the crack propagation rate $\Delta c/\Delta N$ of the equilibrated gel is much smaller than that of the as-prepared gel, demonstrating that the fast self-recovery caused by the noncovalent interactions (ionic bonds in PA gels) slows down the extension of the crack under fatigue test. This can be explained that the noncovalent interactions in self-recovery systems reduce local stress concentrations in front of a propagating crack and reduce the elastic energy transferred to the crack tip (*43*).

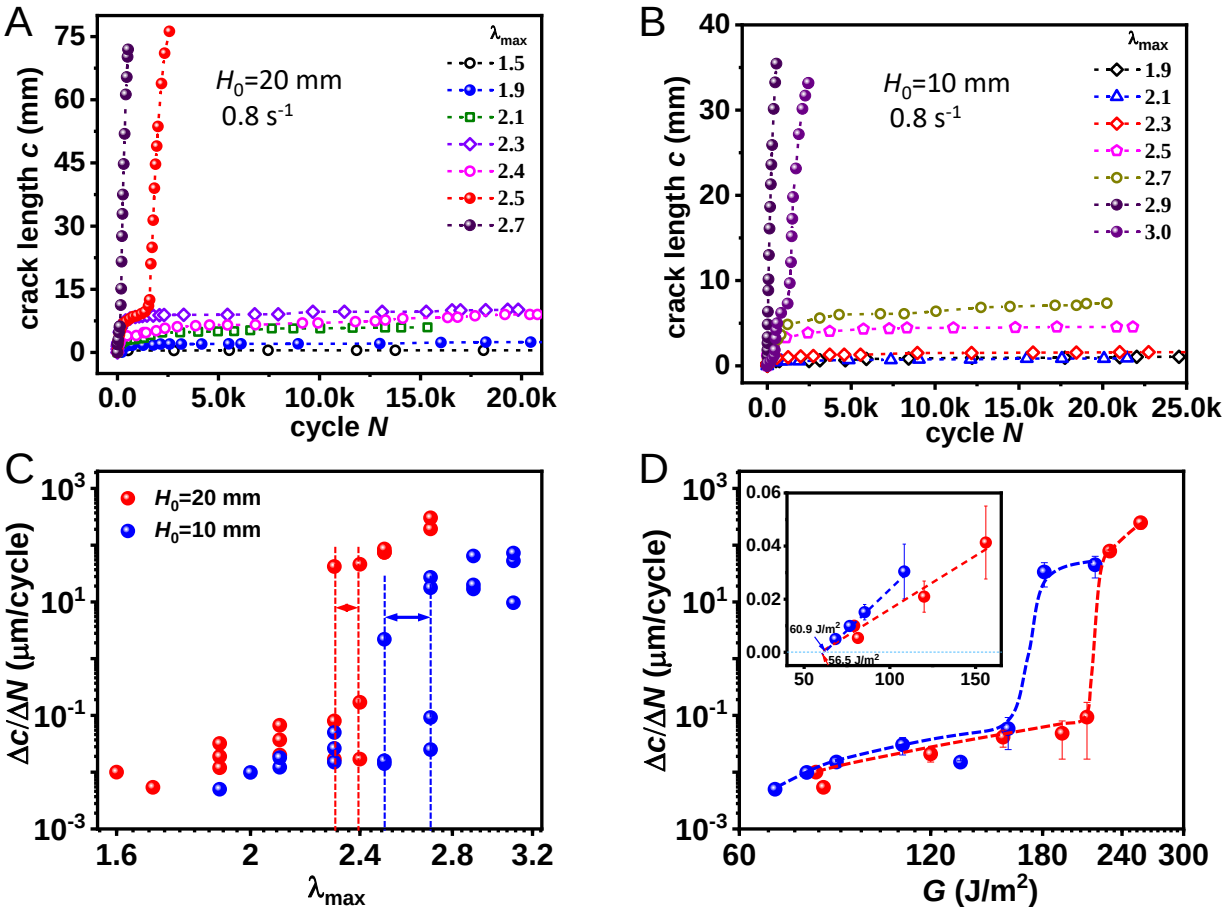

Fig. S6. Geometry effect on fatigue behaviors. Sample with the pure shear geometry drawn in the inset of **Fig. 5A** was applied. The aspect ratios L_0/H_0=5 and c_0/H_0 =1 were kept the same when changing H_0 from H_0=10 mm to H_0=20 mm. A new batch of sample PA-2.0-0.1 is taken as an example (note that the phase structure may be different for samples from different batches). (**A, B**) Crack propagation behavior at different λ_{max} for samples with H_0=20 mm (A) and H_0=10 mm (B). (**C**) Comparison of crack propagation rate $\Delta c/\Delta N$ versus λ_{max} for samples tested in the pure shear geometry at different initial heights H_0. The λ_{tran} are λ_{tran}=2.35±0.05 and λ_{tran}=2.6±0.10 for H_0=20 mm and H_0=10 mm, respectively. The value of λ_{tran} is the middle point of the slow-to-fast transition regime (indicated by the corresponding color of dotted line and arrow) and the error bar of λ_{tran} is the half width of this transition regime. (**D**) The crack propagation rate $\Delta c/\Delta N$ versus energy release rate G in logarithmic scale. Symbols in (D) are the same as those in (C). Inset shows the initial regime in the linear scale, and the fatigue threshold G_0 (indicated by arrow) is obtained by linearly extrapolating the results to the horizontal axis. The G_0 for the two H_0 is almost the same (G_0=60.9 J/m^2 and 56.5 J/m^2 for H_0=10 mm and 20 mm, respectively). The G_{tran} corresponding to the energy release rate at λ_{tran} are G_{tran}=202.3±9.1 J/m^2 and G_{tran}=142.1±15.3 J/m^2 for H_0=20 mm and H_0=10 mm, respectively. In **Fig. S6D,** the $\Delta c/\Delta N$ is the average values of points in **Fig. S6C** at the corresponding λ_{max}, and the $\Delta c/\Delta N$ in the slow-to-fast transition regime was obtained from the statistical average values of the high probability mode at the corresponding λ_{max} (the $\Delta c/\Delta N$ in **Fig. 4A-4D** and **Fig. 5B** was also obtained by this method). In this experiment, a nominal strain rate of 0.8 s^{-1} was used due to the limits of the crosshead speed of the tensile machine (1000 mm/min).

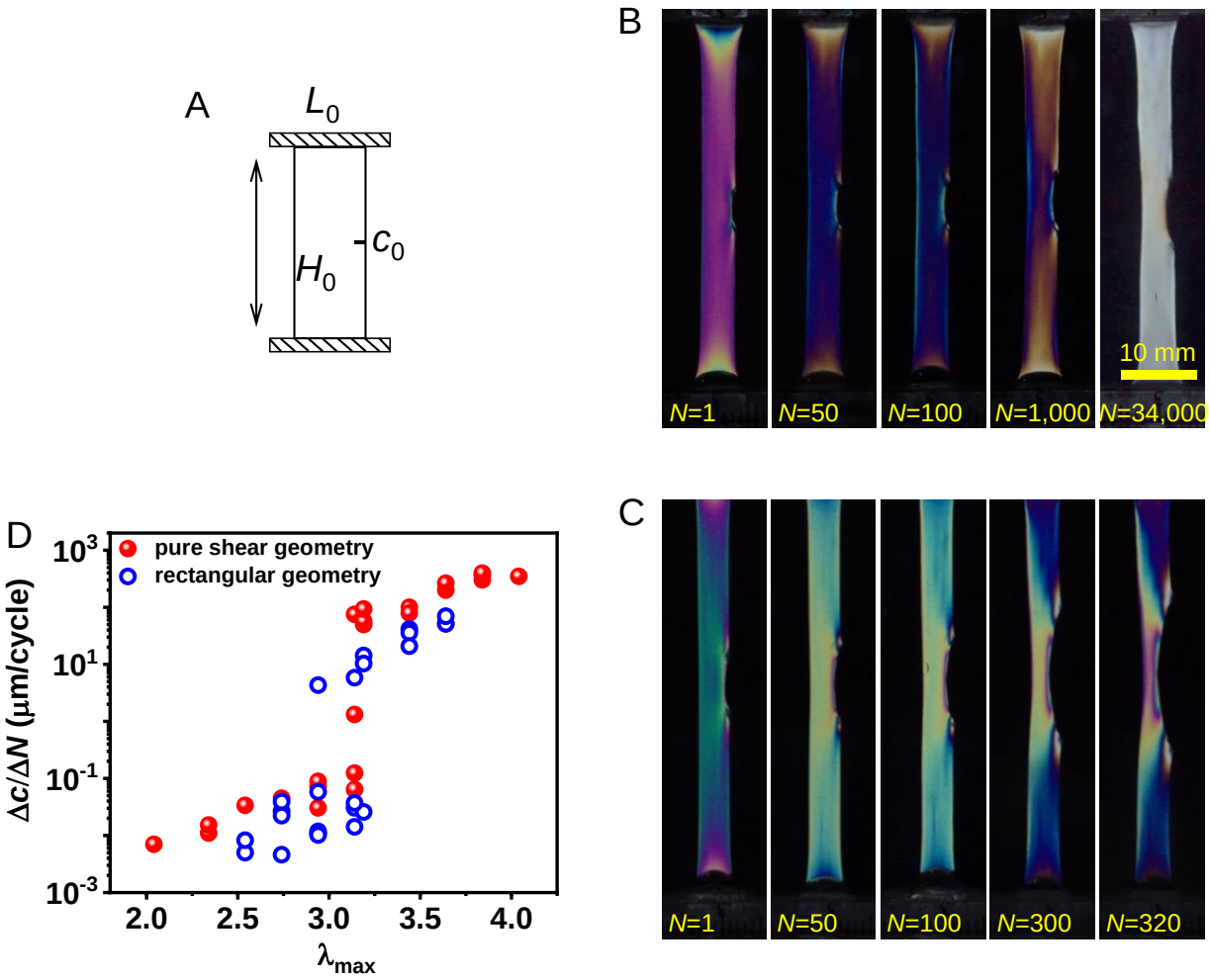

Fig. S7. Fatigue behavior of sample with rectangular geometry. Here takes PA-2.0-0.1 as an example. (**A**) Rectangular geometry (L_0=7.5 mm, H_0=16 mm, and c_0=1 mm). (**B**, **C**) Evolution of birefringence patterns with increasing fatigue cycles N at $\lambda_{max}=2.94<\lambda_{tran}$ (B) and at $\lambda_{max}=3.44>\lambda_{tran}$ (C). (**D**) crack propagation rate $\Delta c/\Delta N$ as a function of λ_{max} for PA-2.0-0.1 tested in a pure shear geometry (L_0=50 mm, H_0=10 mm, and c_0=10 mm) and the rectangular geometry.

Coincide with the results shown in **Fig. 3D** and **3E**, the stress concentration around crack tip is also gradually eliminated with increasing fatigue cycles N at slow crack propagation mode, that is $\lambda_{max}<\lambda_{tran}$, resulting in crack blunting (**Fig. S7B**); while the stress concentration becomes more severe with increasing fatigue cycles N at $\lambda_{max}>\lambda_{tran}$, resulting in relatively sharp crack tip (**Fig. S7C**). Most importantly, rectangular sample shows a slow-to-fast crack propagation transition at $\lambda_{tran}=3.07\pm0.13$ (**Fig. S7D**), very close to that of pure shear geometry ($\lambda_{tran}=3.14$). The data of sample in the pure shear geometry in **Fig. S7D** were extracted from (*25*).

3. Deducing scaling relation between G_0 and ξ based on the Lake-Thomas model

According to Lake-Thomas theory (*44*), threshold G_0 is related to mesh size of permanent polymer network ξ by

$$G_0 = A\nu_e N_{x,eff} U_b \xi, \quad \text{(SM-7)}$$

where $N_{x,eff}$ is the average number of repeat units between the effective permanent cross-linking points, since the trapped topological entanglements also contribute to G_0 as indicated in main text. U_b is the bond energy. $\nu_e \cong \xi^{-3}$ is the effective permanent cross-linking chain density of the network. A is a pre-factor. Since the PA strands are in collapsed globule state (*26, 50*), we have

$$\xi \sim N_{x,eff}^{1/3}. \quad \text{(SM-8)}$$

Thus, we can write

$$G_0 \sim \xi. \quad \text{(SM-9)}$$

4. Estimate of the number of entanglements for the physical PA gel.

For the PA gel prepared with no chemical cross-linker (PA-2.5-0), it fully dissolves in concentrated NaCl (4M) at elevated temperature, indicating that the PA-2.5-0 is a pure physical gel, not containing any chemical cross-linking by any side chemical reaction. The average molecular mass M of linear PA chains was estimated from the overlapping concentration C^* of the polymer solution, where the viscosity increased dramatically (*7*). The PA-2.5-0 gel was dissolved in 4 M saline solution at 55°C for 2 days, then we obtained homogeneous aqueous solution. The overlap concentration determined by the specific viscosity in 4 M saline solution was $C^* \approx 10$ g/L (**Fig. S8**), corresponding to the repeat unit concentration ≈ 0.05 mol/L. C^* is related to the average degree of polymerization N and the coil size of a polymer chain R as

$$C^* \sim \frac{N}{N_A \frac{4}{3}\pi R^3}, \qquad \text{(SM-10)}$$

where, the N_A is Avogadro constant (6.02×10^{23} mol^{-1}). Assuming that the polymer in 4 M NaCl solution is in the Θ solvent, $R^2 = C_\infty a^2 N$, where a (~ 0.15 nm) is the repeat unit size and C_∞ is a number related to the local stiffness of a polymer chain (typical values are 7-9 for flexible polymers (*26*)), Thus, we have

$$N \sim \left(\frac{3}{4N_A \pi a^3 C^*}\right)^2 C_\infty^{-3}. \qquad \text{(SM-11)}$$

Taking a value $C_\infty = 7$ for flexible polymers, the degree of polymerization is $N \sim 1.6\times10^4$, and the corresponding molecular mass is around $M \sim 3.2\times10^6$ g/mol for the chains of physical gel PA-2.5-0. The molar mass of polymer strands between entanglements M_e, was evaluated from the quasi-plateau modulus (G_e), by using $G_e \approx \rho\phi RT/M_e$, as described in Section S2.1. The value of M_e for gel PA-2.5-0 is 197.5×10^3 g/mol, as presented in **Table S1.** The number of topological entanglements per linear chain of PA-2.5-0.1 is estimated as ~16 from the ratio M/M_e.

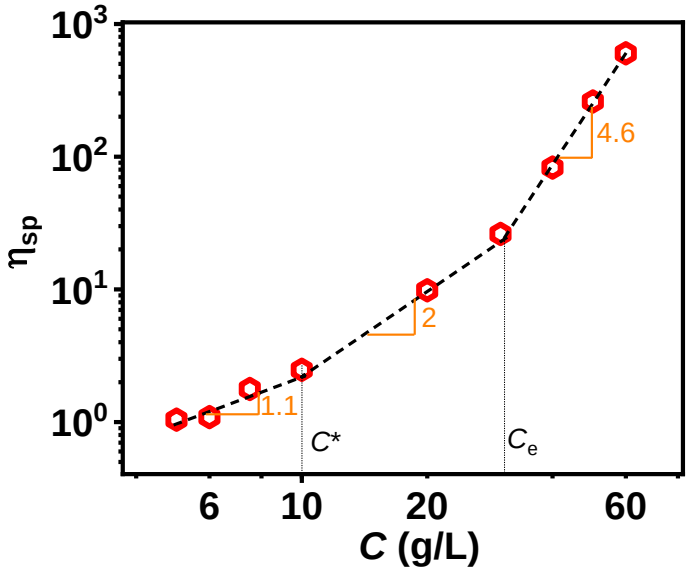

Fig. S8. Concentration dependence of specific viscosity η_{sp} for pure physical gel PA-2.5-0 dissolved in 4 M saline solution. From the plot, we can get the overlap concentration $C^* \approx 10$ g/L.

Movie S1. Stress concentration around crack tip is reduced with cycle number N for the strongly phase-separated gel when fatigue test is performed at $\lambda_{max}<\lambda_{tran}$, resulting in crack blunting and extremely slow crack propagation. Gel PA-2.5-0.075 with high phase contrast at $\lambda_{max}=2.64$ is taken as an example. The movie plays at 2 times of real-time speed.

Movie S2. Severe stress concentration around crack tip persists for the strongly phase-separated gel when fatigue test is performed at $\lambda_{max}>\lambda_{tran}$, resulting in rapid crack propagation. Gel PA-2.5-0.075 with high phase contrast at $\lambda_{max}=3.44$ is taken as an example. The movie plays at 2 times of real-time speed.

Movie S3. Severe stress concentration around crack tip persists for the weakly phase-separated gel when fatigue test is performed at a very small λ_{max}, resulting in rapid crack propagation. Gel PA-2.5-0.5 with low phase contrast at $\lambda_{max}=1.81$ is taken as an example. The movie plays at 2 times of real-time speed.

REFERENCES AND NOTES

1. J. J. Green, J. H. Elisseeff, Mimicking biological functionality with polymers for biomedical applications. *Nature* **540**, 386–394 (2016).

2. M. A. Haque, T. Kurokawa, J. P. Gong, Super tough double network hydrogels and their application as biomaterials. *Polymer* **53**, 1805–1822 (2012).

3. J. P. Gong, Y. Katsuyama, T. Kurokawa, Y. Osada, Double-network hydrogels with extremely high mechanical strength. *Adv. Mater.* **15**, 1155–1158 (2003).

4. J. P. Gong, Why are double network hydrogels so tough? *Soft Matter* **6**, 2583 (2010).

5. J. P. Gong, Materials both tough and soft. *Science* **344**, 161–162 (2014).

6. Y. S. Zhang, A. Khademhosseini, Advances in engineering hydrogels. *Science* **356**, eaaf3627 (2017).

7. T. L. Sun, T. Kurokawa, S. Kuroda, A. B. Ihsan, T. Akasaki, K. Sato, M. A. Haque, T. Nakajima, J. P. Gong, Physical hydrogels composed of polyampholytes demonstrate high toughness and viscoelasticity. *Nat. Mater.* **12**, 932–937 (2013).

8. J.-Y. Sun, X. Zhao, W. R. Illeperuma, O. Chaudhuri, K. H. Oh, D. J. Mooney, J. J. Vlassak, Z. Suo, Highly stretchable and tough hydrogels. *Nature* **489**, 133–136 (2012).

9. X. Dai, Y. Zhang, L. Gao, T. Bai, W. Wang, Y. Cui, W. Liu, A mechanically strong, highly stable, thermoplastic, and self-healable supramolecular polymer hydrogel. *Adv. Mater.* **27**, 3566–3571 (2015).

10. W. Wang, Y. Zhang, W. Liu, Bioinspired fabrication of high strength hydrogels from non-covalent interactions. *Prog. Polym. Sci.* **71**, 1–25 (2017).

11. R. Bai, J. Yang, X. P. Morelle, C. Yang, Z. Suo, Fatigue fracture of self-recovery hydrogels. *ACS Macro Lett.* **7**, 312–317 (2018).

12. R. Bai, Q. Yang, J. Tang, X. P. Morelle, J. Vlassak, Z. Suo, Fatigue fracture of tough hydrogels. *Extr. Mech. Lett.* **15**, 91–96 (2017).

13. R. Bai, J. Yang, Z. Suo, Fatigue of hydrogels. *Eur. J. Mech. Solid* **74**, 337–370 (2019).

14. M. A. Meyers, J. McKittrick, P.-Y. Chen, Structural biological materials: Critical mechanics-materials connections. *Science* **339**, 773–779 (2013).

15. U. G. Wegst, H. Bai, E. Saiz, A. P. Tomsia, R. O. Ritchie, Bioinspired structural materials. *Nat. Mater.* **14**, 23–36 (2015).

16. S. Lin, X. Liu, J. Liu, H. Yuk, H.-C. Loh, G. A. Parada, C. Settens, J. Song, A. Masic, G. H. McKinley, X. Zhao, Anti-fatigue-fracture hydrogels. *Sci. Adv.* **5**, eaau8528 (2019).

17. S. Lin, J. Liu, X. Liu, X. Zhao, Muscle-like fatigue-resistant hydrogels by mechanical training. *Proc. Natl. Acad. Sci. U.S.A.* **116**, 10244–10249 (2019).

18. J. Liu, S. Lin, X. Liu, Z. Qin, Y. Yang, J. Zang, X. Zhao, Fatigue-resistant adhesion of hydrogels. *Nat. Commun.* **11**, 1071 (2020).

19. C. Li, H. Yang, Z. Suo, J. Tang, Fatigue-resistant elastomers. *J. Mech. Phys. Solids* **134**, 103751 (2020).

20. G. Su, J. Cao, X. Zhang, Y. Zhang, S. Yin, L. Jia, Q. Guo, X. Zhang, J. Zhang, T. Zhou, Human-tissue-inspired anti-fatigue-fracture hydrogel for a sensitive wide-range human–machine interface. *J. Mater. Chem. A* **8**, 2074–2082 (2020).

21. C. Xiang, Z. Wang, C. Yang, X. Yao, Y. Wang, Z. Suo, Stretchable and fatigue-resistant materials. *Mater. Today* **34**, 7–16 (2020).

22. X. Zhao, EML webinar overview: Extreme mechanics of soft materials for merging human-machine intelligence. *Extr. Mech. Lett.* **39**, 100784 (2020).

23. K. Cui, T. L. Sun, X. Liang, K. Nakajima, Y. N. Ye, L. Chen, T. Kurokawa, J. P. Gong, Multiscale energy dissipation mechanism in tough and self-healing hydrogels. *Phys. Rev. Lett.* **121**, 185501 (2018).

24. K. Cui, Y. N. Ye, T. L. Sun, C. Yu, X. Li, T. Kurokawa, J. P. Gong, Phase separation behavior in tough and self-healing polyampholyte hydrogels. *Macromolecules* **53**, 5116–5126 (2020).

25. X. Li, K. Cui, T. L. Sun, L. Meng, C. Yu, L. Li, C. Creton, T. Kurokawa, J. P. Gong, Mesoscale bicontinuous networks in self-healing hydrogels delay fatigue fracture. *Proc. Natl. Acad. Sci. U.S.A.* **117**, 7606–7612 (2020).

26. M. Rubinstein, R. H. Colby, *Polymer Physics* (Oxford Univ. Press, 2003).

27. S. H. Yoo, L. Yee, C. Cohen, Effect of network structure on the stress-strain behaviour of endlinked PDMS elastomers. *Polymer* **51**, 1608–1613 (2010).

28. T. L. Sun, F. Luo, T. Kurokawa, S. N. Karobi, T. Nakajima, J. P. Gong, Molecular structure of self-healing polyampholyte hydrogels analyzed from tensile behaviors. *Soft Matter* **11**, 9355–9366 (2015).

29. P. G. Higgs, J. F. Joanny, Theory of polyampholyte solutions. *J. Chem. Phys.* **94**, 1543–1554 (1991).

30. L. Boldon, F. Laliberte, L. Liu, Review of the fundamental theories behind small angle X-ray scattering, molecular dynamics simulations, and relevant integrated application. *Nano Rev.* **6**, 25661 (2015).

31. T.-T. Mai, K. Okuno, K. Tsunoda, K. Urayama, Crack-tip strain field in supershear crack of elastomers. *ACS Macro Lett.* **9**, 762–768 (2020).

32. T. Zhang, S. Lin, H. Yuk, X. Zhao, Predicting fracture energies and crack-tip fields of soft tough materials. *Extr. Mech. Lett.* **4**, 1–8 (2015).

33. S. Mzabi, D. Berghezan, S. Roux, F. Hild, C. Creton, A critical local energy release rate criterion for fatigue fracture of elastomers. *J. Polym. Sci. B* **49**, 1518–1524 (2011).

34. R. Long, C.-Y. Hui, J. P. Gong, E. Bouchbinder, The fracture of highly deformable soft materials: A tale of two length scales. *Annu. Rev. Cond. Matter Phys.* **12**, 104028 (2020).

35. R. S. Rivlin, A. G. Thomas, Rupture of rubber. I. Characteristic energy for tearing. *J. Polym. Sci.* **10**, 291–318 (1953).

36. T. Matsuda, R. Kawakami, T. Nakajima, J. P. Gong, Crack tip field of a double-network gel: Visualization of covalent bond scission through mechanoradical polymerization. *Macromolecules* **53**, 8787–8795 (2020).

37. E. Ducrot, Y. Chen, M. Bulters, R. P. Sijbesma, C. Creton, Toughening elastomers with sacrificial bonds and watching them break. *Science* **344**, 186–189 (2014).

38. P. Millereau, E. Ducrot, J. M. Clough, M. E. Wiseman, H. R. Brown, R. P. Sijbesma, C. Creton, Mechanics of elastomeric molecular composites. *Proc. Natl. Acad. Sci. U.S.A.* **115**, 9110–9115 (2018).

39. W. Cui, D. R. King, Y. Huang, L. Chen, T. L. Sun, Y. Guo, Y. Saruwatari, C. Y. Hui, T. Kurokawa, J. P. Gong, Fiber-reinforced viscoelastomers show extraordinary crack resistance that exceeds metals. *Adv. Mater.* **32**, e1907180 (2020).

40. W. Zhang, J. Hu, J. Tang, Z. Wang, J. Wang, T. Lu, Z. Suo, Fracture toughness and fatigue threshold of tough hydrogels. *ACS Macro Lett.* **8**, 17–23 (2019).

41. Y. Zhou, W. Zhang, J. Hu, J. Tang, C. Jin, Z. Suo, T. Lu, The stiffness-threshold conflict in polymer networks and a resolution. *J. Appl. Mech.* **87**, 031002 (2020).

42. W. Zhang, X. Liu, J. Wang, J. Tang, J. Hu, T. Lu, Z. Suo, Fatigue of double-network hydrogels. *Eng. Fract. Mech.* **187**, 74–93 (2018).

43. C. Creton, 50th anniversary perspective: Networks and gels: Soft but dynamic and tough. *Macromolecules* **50**, 8297–8316 (2017).

44. G. Lake, A. Thomas, The strength of highly elastic materials. *Proc. R. Soc. Lond. A Math. Phys. Sci.* **300**, 108–119 (1967).

45. I. Naassaoui, O. Ronsin, T. Baumberger, A poroelastic signature of the dry/wet state of a crack tip propagating steadily in a physical hydrogel. *Extr. Mech. Lett.* **22**, 8–12 (2018).

46. A. B. Ihsan, T. L. Sun, T. Kurokawa, S. N. Karobi, T. Nakajima, T. Nonoyama, C. K. Roy, F. Luo, J. P. Gong, Self-healing behaviors of tough polyampholyte hydrogels. *Macromolecules* **49**, 4245–4252 (2016).

47. F. Luo, T. L. Sun, T. Nakajima, T. Kurokawa, Y. Zhao, A. B. Ihsan, H. L. Guo, X. F. Li, J. P. Gong, Crack blunting and advancing behaviors of tough and self-healing polyampholyte hydrogel. *Macromolecules* **47**, 6037–6046 (2014).

48. Z. Gao, K. Lister, J. P. Desai, Constitutive modeling of liver tissue: Experiment and theory. *Ann. Biomed. Eng.* **38**, 505–516 (2010).

49. R. Long, C.-Y. Hui, Fracture toughness of hydrogels: Measurement and interpretation. *Soft Matter* **12**, 8069–8086 (2016).

50. A. V. Dobrynin, R. H. Colby, M. Rubinstein, Polyampholytes. *J. Polym. Sci. B* **42**, 3513–3538 (2004).